# Two-stage Optimal Scheduling of Community Integrated Energy System Considering Operation Sequences of Hydrogen Energy Storage Systems

Wei Kong, Kai Sun, and Jinghong Zhao

***Abstract*—The hydrogen energy storage system (HESS) integrated with renewable energy power generation exhibits low reliability and flexibility under source-load uncertainty. To address the above issues, a two-stage optimal scheduling model considering the operation sequences of HESSs is proposed for commercial community integrated energy systems (CIESs) with power to hydrogen and heat (P2HH) capability. It aims to optimize the energy flow of HESS and improve the flexibility of hydrogen production and the reliability of energy supply for loads. First, the refined operation model of HESS is established, and its operation model is linearized according to the operation domain of HESS, which simplifies the difficulty of solving the optimization problem under the premise of maintaining high approximate accuracy. Next, considering the flexible start-stop of alkaline electrolyzer (AEL) and the avoidance of multiple energy conversions, the operation sequences of HESS are formulated. Finally, a two-stage optimal scheduling model combining day-ahead economic optimization and intra-day rolling optimization is established, and the model is simulated and verified using the source-load prediction data of typical days in each season. The simulation results show that the two-stage optimal scheduling reduces the total load offset by about 14% while maintaining similar operating cost to the optimal day-ahead economic optimization scheduling. Furthermore, by formulating the operation sequences of HESS, the operating cost of CIES is reduced by up to about 4.4%.**

***Index Terms*—Community integrated energy system (CIES), hydrogen storage, operation sequence, two-stage optimal scheduling.**

## I. Introduction

CONVENTIONAL commercial communities have problems such as high energy demand, high power supply reliability requirement, low energy utilization efficiency, poor economic benefits, and severe environmental pollution [1]. The community integrated energy system (CIES) is used to reduce carbon emissions and improve energy efficiency because it includes various forms of clean energy. Electric energy is typically used to realize the coupling of multiple energy sources to change the energy supply of the community from the multi-energy independent supply mode to the multi-energy joint supply mode, which is convenient for the unified planning and economic optimization of CIES [2].

With the development of hydrogen energy technologies such as electrolytic water hydrogen production and hydrogen fuel cells, hydrogen energy can be used as a clean multi-purpose terminal energy source [3]. By introducing the hydrogen energy storage system (HESS) into the CIES, the direct use of distributed renewable energy power generation or the valley-price power from the grid to electrolyze water to produce hydrogen can satisfy the hydrogen demand of the local hydrogen load, which can reduce hydrogen purchase and transportation costs and achieve low-carbon emission.

CIES with hydrogen energy storage is highly complex and coupled with various energy flows. It is critical to coordinate and optimize the operation of various power sources and loads to ensure the reliability and economy of the system operation. The energy management system (EMS) of CIES includes two methods: online strategy control [4]-[7] and optimal energy scheduling [8]-[15]. In [4], reliable grid-connected renewable power generation was achieved by the coordinated control of the hydrogen energy storage and supercapacitor. In [5], the system cost was reduced using the fuzzy logic algorithm. The adaptive network-based fuzzy inference system (ANFIS) based on fuzzy control and neural network was studied in [6]. In [7], model predictive control (MPC) was used to realize the online optimal dynamic control of the electro-hydrogen coupling system. EMS based on online strategies can achieve online optimization but may not necessarily be the optimal solution. In [8], the optimal scheduling of a regional electro-hydrogen coupling system was studied to minimize the cost of hydrogen production. In [10], the design and day-ahead economic optimization scheduling of zero-emission buildings with the HESS were investigated. In [11], the beluga whale optimization algorithm was used to solve the day-ahead economic optimization energy scheduling of the zero-carbon community with the HESS and fuel-cell electric vehicles (FCEVs). The optimal day-ahead economic optimization scheduling considering the thermoelec-

Manuscript received: January 2, 2024; revised: May 7, 2024; accepted: July 4, 2024. Date of CrossCheck: July 4, 2024. Date of online publication: July 29, 2024.

This work was supported by the Major Science and Technology Innovation Project of Jiangsu Province of China (No. BE2022038).



W. Kong and J. Zhao are with the School of Electrical Engineering, Naval University of Engineering, Wuhan, China (e-mail: sdytkongwei@163.com; zhaojinghong@163.com).

K. Sun (corresponding author) is with the Department of Electrical Engineering, State Key Laboratory of Power System Operation and Control, Tsinghua University, Beijing, China (e-mail: sun-kai@mail.tsinghua.edu.cn).

DOI: 10.35833/MPCE.2023.001027

tric performance and state transition of alkaline electrolyzer (AEL) was studied in [12]. In [13], the optimal energy scheduling of the regionally integrated energy system was studied to explain the benefits of introducing a complete hydrogen industry chain. The influence of waste heat recovery of proton exchange membrane fuel cell (PEMFC) on the optimal scheduling economy of integrated energy systems has been studied in [14], [15].

Ensuring the flexible and economic operation of CIES containing hydrogen energy storage under the uncertainty of renewable power generation and load is the critical problem for the economic scheduling. The hybrid energy scheduling algorithm of the hydrogen microgrid based on the deep deterministic policy gradient was studied to cope with the influence of source-load uncertainty in [16]. The day-ahead robust optimal scheduling of CIES was studied in [17], [18]. The optimal scheduling of a regional integrated energy system based on scenario analysis was studied in [19]. In [20], a two-stage optimal scheduling model of integrated energy system was established. However, some optimal scheduling models including HESS do not consider the start-stop constraints of AEL and the optimization of energy flow within the system, which affects the reliability and economy of scheduling. In addition, the nonlinear operation characteristics of the HESS also bring difficulties to the optimal scheduling calculation of the CIES. In [12], in order to simplify the optimization, the tangent plane method was used to linearize the power-current density relationship of AEL. In [21], the hydrogen production rate of AEL was linearly fitted. In [15] and [22], the hydrogen consumption rate of PEMFC was regarded as a constant, and the auxiliary power consumption was not considered. However, there is a lack of linearized models that facilitate the direct use of HESSs in scheduling, including electric power and heat generation power, electric power and hydrogen production rate, and electric power and hydrogen consumption rate. Additionally, the power consumption of PEMFC auxiliary equipment cannot be ignored. In response to the current research issues mentioned above, this paper proposes a refined two-stage optimal scheduling model considering the operation sequences of HESS. The contributions of this paper are as follows:

1) The refined model of HESS is established and linearized according to the operation domain, which simplifies the difficulty of solving the optimization problem while ensuring sufficient accuracy.

2) The operation sequences of HESS are designed for the rapid start-up of AEL and the optimization of energy flow path within the system, which improve the flexibility and economy of HESS operation.

3) A refined two-stage optimal scheduling model of CIES containing hydrogen energy storage is established. In the economic optimization objective function, the life decline cost and start-stop cost of HESS are considered. Under the constraint conditions, the loss of hydrogen purification, the standby power consumption, and the operation sequences of AEL are considered. The established scheduling model can simulate the operation of the actual system more accurately and improve the reliability and economy of the CIES.

The rest of this paper is organized as follows. In Section II, the architecture and parameter configuration of CIES with power to hydrogen and heat (P2HH) are introduced. In Section III, the operation model of CIES is established. In Section IV, the operation sequences of HESS are formulated. In Section V, the model and constraints of two-stage optimal scheduling are introduced. In Section VI, the proposed optimal scheduling model is simulated and verified. Finally, the conclusion is summarized in Section VII.

## II. Architecture and Parameter Configuration of CIES with P2HH

Figure 1 displays the architecture of CIES with P2HH, which comes from an actual community of office buildings. It mainly includes distributed photovoltaic (PV) power generation system, HESS, battery energy storage system (BESS), electric boiler, EMS, and electric-hydrogen-heat load.

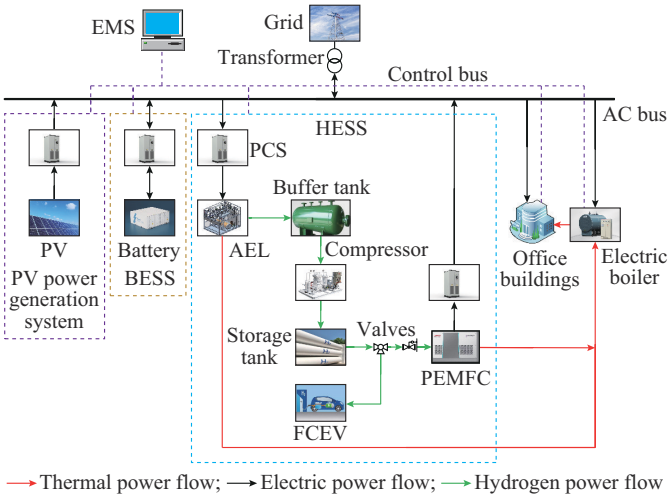


Fig. 1. Architecture of CIES with P2HH.

The electric load in the CIES mainly includes air conditioning and lighting. The heat load is the hot water supply demand in the CIES. The hydrogen load is the hydrogenation demand of a commercial hydrogen FCEV with a hydrogen energy storage capacity of 20 kg, which helps realize a low-carbon emission community. The FCEV is filled with hydrogen through a hydrogenation machine with a working pressure of 35 MPa and a filling rate of 0-2 kg/min. The direct hydrogen filling time is approximately 10-15 min. According to the design specification of the hydrogen refueling station, the 35 MPa hydrogen refueling station can be configured with a 45 MPa high-pressure hydrogen storage tank. The volume of the storage tank is 5 $m^3$, and the effective hydrogen storage mass is 114 kg. Considering the energy requirements in the CIES, the installed capacity of distributed PV is 700 kW, and the maximum power and capacity of BESS are 1 MW and 2 MWh, respectively. The CIES is equipped with an electric boiler of 200 kW rated power as the primary heat source. The system is equipped with an AEL with a rated hydrogen production rate of 40 $N \cdot m^3/h$, and the total amount of hydrogen production can reach 85 kg in a day at full load. At the same time, in order to en-

hance the resilience of CIES against unplanned power outages of the utility grid, a fixed PEMFC with a rated power of 77 kW is also equipped, which can be used for energy replenishment of the system during high electricity price time under normal operating conditions as well. Because of the existence of multiple energy requirements of electric energy, heat energy, and hydrogen energy in the CIES, and lower electrical efficiency of AEL and hydrogen fuel cell under heavy load, the waste heat recovery systems of AEL and PEMFC are added to further improve the comprehensive energy utilization rate of the system. The HESS is composed of AEL, hydrogen compressor, hydrogen storage tank, and fixed PEMFC. The functions of EMS include source-load data prediction and optimal scheduling.

## III. Operation Model of CIES

Before establishing the optimal scheduling model, establishing the operation models of each subsystem of the CIES is critical for accurately describing their operating characteristics.

### A. Operation Model of AEL

According to the principle of the electrochemical reaction of AEL [23], [24], the operating voltage of AEL can be expressed as:

$$U_{\mathrm{ael}} = \left(U_{\mathrm{rev}}^{\mathrm{ael}} + U_{\mathrm{ohm}}^{\mathrm{ael}} + U_{\mathrm{act}}^{\mathrm{ael}}\right) N_{\mathrm{s}}^{\mathrm{ael}} \tag{1}$$

$$U_{\mathrm{rev}}^{\mathrm{ael}} = 1.5184 - 1.5421\times10^{-3}T_{\mathrm{ael}} + 9.526\times10^{-5}T_{\mathrm{ael}}\ln\left(T_{\mathrm{ael}}\right) + 9.84\times10^{-8}T_{\mathrm{ael}}^{2} + \frac{RT_{\mathrm{ael}}}{2F}\ln\left(\frac{\left(P-P_{\mathrm{H_2O}}\right)^{1.5}}{\alpha_{\mathrm{H_2O}}}\right) \tag{2}$$

$$U_{\mathrm{ohm}}^{\mathrm{ael}} = \left(r_1 + r_2 t_{\mathrm{ael}}\right) J_{\mathrm{ael}} \tag{3}$$

$$U_{\mathrm{act}}^{\mathrm{ael}} = \left(s_1 + s_2 t_{\mathrm{ael}} + s_3 t_{\mathrm{ael}}^{2}\right)\lg\left(\left(t_1 + \frac{t_2}{t_{\mathrm{ael}}} + \frac{t_3}{t_{\mathrm{ael}}^{2}}\right) J_{\mathrm{ael}} + 1\right) \tag{4}$$

where $R$ is the standard gas constant; $P$ is the working pressure; $P_{\mathrm{H_2O}}$ is the partial pressure of water vapor; $U_{\mathrm{rev}}^{\mathrm{ael}}$ is the reversible overvoltage corrected by the temperature and pressure; $U_{\mathrm{ohm}}^{\mathrm{ael}}$ is the ohmic overvoltage; $U_{\mathrm{act}}^{\mathrm{ael}}$ is the electrode activation overvoltage; $N_{\mathrm{s}}^{\mathrm{ael}}$ is the number of cells in the AEL; $T_{\mathrm{ael}}$ and $t_{\mathrm{ael}}$ are the Kelvin temperature and Celsius temperature, respectively; $F$ is the Faraday constant; $\alpha_{\mathrm{H_2O}}$ is the activity of water; $r_1$ and $r_2$ are the ohmic overvoltage coefficients of AEL, which represent the ohmic resistance of membrane electrode in the electrolyzer; $s_1$-$s_3$ and $t_1$-$t_3$ are the electrode activation overvoltage coefficients of AEL, which represent the energy loss caused by overcoming the electrode activation energy; and $J_{\mathrm{ael}}$ is the operating current density.

According to Faraday law, the hydrogen production rate of AEL is as follows:

$$N_{\mathrm{H_2}} = \eta_{\mathrm{F}}\frac{3.6\times22.4N_{\mathrm{s}}^{\mathrm{ael}}J_{\mathrm{ael}}A}{2F} \tag{5}$$

$$\eta_{\mathrm{F}} = a_1\mathrm{e}^{\left(\frac{a_2+a_3t_{\mathrm{ael}}}{J_{\mathrm{ael}}} + \frac{a_4+a_5t_{\mathrm{ael}}}{J_{\mathrm{ael}}^{2}}\right)} \tag{6}$$

where $N_{\mathrm{H_2}}$ is the hydrogen production rate; $\eta_{\mathrm{F}}$ is the Faraday efficiency; $a_1$-$a_5$ are the Faraday efficiency coefficients, which represent the hydrogen loss caused by parasitic current in the electrolyzer; and $A$ is the active area of the electrode.

The electric power consumed by hydrogen production in the AEL is as follows:

$$P_{\mathrm{ael}} = U_{\mathrm{ael}}J_{\mathrm{ael}}A \tag{7}$$

According to [24], the heat generation power of AEL can be expressed as:

$$Q_{\mathrm{ael}} = \left(U_{\mathrm{ael}} - U_{\mathrm{tn}}\right)J_{\mathrm{ael}}A \tag{8}$$

where $U_{\mathrm{tn}}$ is the thermal neutral voltage.

The thermal power that the waste heat recovery system can recover from the AEL is as follows:

$$Q_{\mathrm{ael}}^{\mathrm{rec}} = \left(Q_{\mathrm{ael}} - Q_{\mathrm{dis}}^{\mathrm{ael}}\right)\eta_{\mathrm{rec}} \tag{9}$$

where $\eta_{\mathrm{rec}}$ is the waste heat recovery efficiency; and $Q_{\mathrm{dis}}^{\mathrm{ael}}$ is the dissipated heat power of AEL to the surrounding environment.

The technical parameters of the ZDQ40 commercial AEL, as shown in Table I, are used for the scheduling simulation. The operating characteristics of AEL are displayed in Fig. 2, where $I_{\mathrm{ael}}$ is the operating current of AEL.

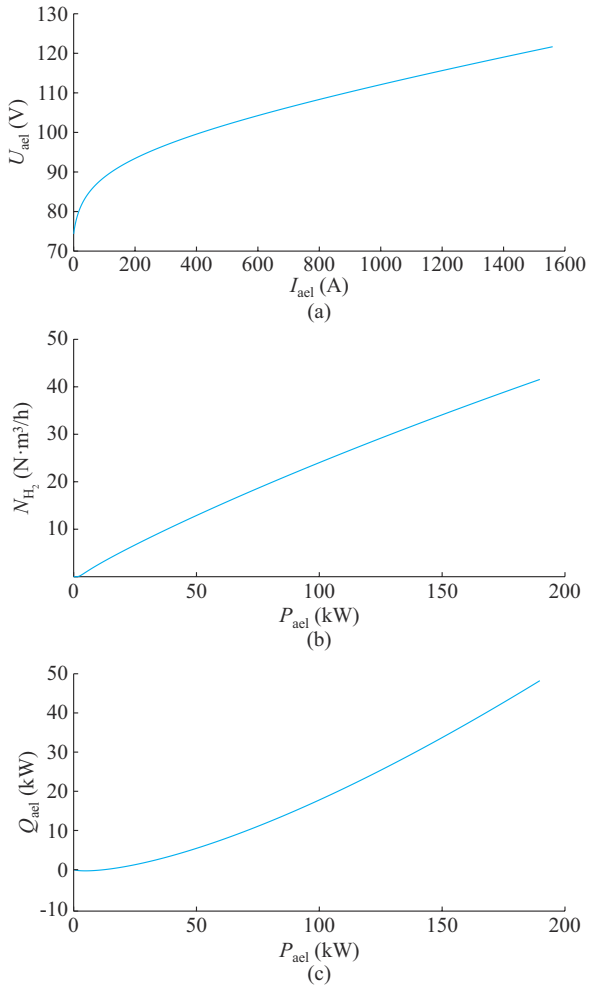


Fig. 2. Operating characteristics of AEL. (a) *U-I* characteristic. (b) Hydrogen production characteristic. (c) Heat generation characteristic.

TABLE I
TECHNICAL PARAMETERS OF ZDQ40 COMMERCIAL AEL

| Parameter | Value |
|---|---|
| Rated hydrogen production rate | 40 N·m$^3$/h |
| Rated power | 190 kW |
| Rated current | 1560 A |
| Operating pressure | 16 bar |
| Operating temperature | 90 °C |
| Operating load range | 50%-100% |
| Number of electrolytic cells | 60 |
| Active area of electrode | 0.5 m$^2$ |
| Stack diameter | 0.96 m |
| Stack surface area | 3.62 m$^2$ |
| Hydrogen purity | ≥99.8% |
| $r_1$ | $11.8\times10^{-5}$ Ω·m$^2$ |
| $r_2$ | $-1.11\times10^{-7}$ Ω·m$^2$·°C |
| $s_1$ | 0.21 V |
| $s_2$ | $1.38\times10^{-3}$ V/°C |
| $s_3$ | $-1.61\times10^{-5}$ V/°C$^2$ |
| $t_1$ | $1.6\times10^{-2}$ m$^2$/A |
| $t_2$ | −1.302 m$^2$·°C/A |
| $t_3$ | $4.21\times10^{2}$ m$^2$·°C$^2$/A |
| $a_1$ | 1.068 |
| $a_2$ | −9.5788 |
| $a_3$ | −0.0555 |
| $a_4$ | 1502.71 |
| $a_5$ | −70.8 |
| $\eta_{rec}$ | 86% |

Figure 2 reveals that the operating characteristics of AEL in the allowable load range are close to the linear relationship. Therefore, the hydrogen production and heat generation characteristics of AEL can be linearized as:

$$N_{H_2}=c_1P_{ael}+d_1 \tag{10}$$

$$Q_{ael}=c_2P_{ael}+d_2 \tag{11}$$

where $c_1$, $c_2$, $d_1$, and $d_2$ are the linear fitting coefficients, which are set as $c_1=0.197$, $d_1=4.3$, $c_2=0.329$, $d_2=-15.3$ in this paper.

The linearized models in (10) and (11) are compared with the original model of AEL in (5) and (8), as shown in Fig. 3. Within the allowable operating load range of AEL, the linearized model can achieve excellent approximation to the original model. The maximum error occurs under light load, with the maximum error rate of the hydrogen production model being less than 2% and the maximum error rate of the heat generation model being less than 5%.

### *B. Operation Model of PEMFC*

According to the principle of the electrochemical reaction of PEMFC [25], [26], the operating voltage of PEMFC can be expressed as:

$$U_{fc}=\left(U_{oc}^{fc}-U_{act}^{fc}-U_{ohm}^{fc}-U_{con}^{fc}\right)N_s^{fc} \tag{12}$$

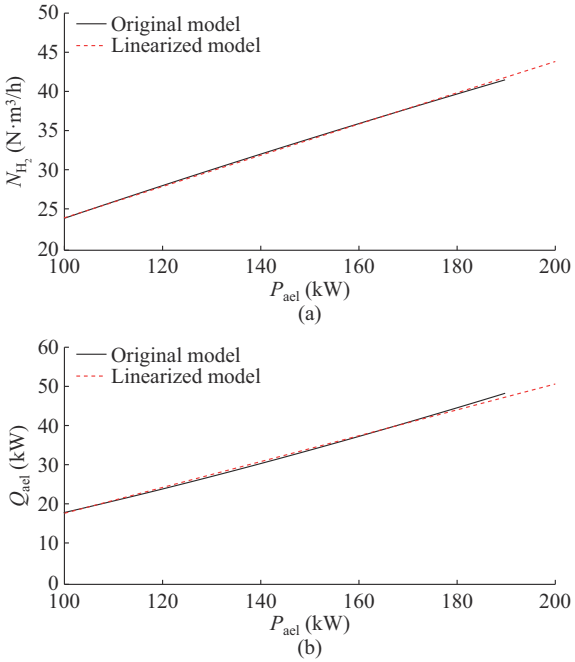


Fig. 3. Comparison of linearized model with original models of AEL. (a) Hydrogen production model. (b) Heat generation model.

$$U_{oc}^{fc}=1.229-0.846\times10^{-3}\left(T_{fc}-T_0\right)+\frac{RT_{fc}}{2F}\ln\left(\frac{P_{H_2}P_{O_2}^{0.5}}{\alpha_{H_2O}}\right) \tag{13}$$

$$U_{act}^{fc}=-\left(f_1+f_2T_{fc}+f_3T_{fc}\ln\left(\frac{P_{O_2}}{5.08\times10^6e^{\frac{-498}{T_{fc}}}}\right)+f_4T_{fc}\ln\left(I_{fc}\right)\right) \tag{14}$$

$$U_{ohm}^{fc}=J_{fc}\cdot ASR \tag{15}$$

$$U_{con}^{fc}=m\cdot10^{-3}e^{1000vJ_{fc}} \tag{16}$$

where $U_{oc}^{fc}$ is the open-circuit voltage of PEMFC; $U_{act}^{fc}$ is the electrode activation overvoltage of PEMFC; $U_{ohm}^{fc}$ is the ohmic overvoltage of PEMFC; $U_{con}^{fc}$ is the concentration overvoltage of PEMFC; $T_{fc}$ is the operating temperature of PEMFC; $T_0$ is the ambient temperature; $P_{H_2}$ is the partial pressure of hydrogen in the anode; $P_{O_2}$ is the partial pressure of oxygen in the cathode; $N_s^{fc}$ is the number of cells in the PEMFC; $J_{fc}$ is the current density of PEMFC; $m$ and $v$ are the concentration overvoltage coefficients of PEMFC; $f_1$-$f_4$ are the electrode activation overvoltage coefficients of PEMFC; $ASR$ is the area-specific resistance; and $I_{fc}$ is the operating current of PEMFC.

The power generation of PEMFC can be obtained according to the hydrogen consumption rate and operating voltage as follows:

$$I_{fc}=\frac{2FW_{H_2}}{60\times22.4N_s^{fc}S_{H_2}} \tag{17}$$

$$P_{fc}=U_{fc}I_{fc} \tag{18}$$

where $W_{H_2}$ is the hydrogen consumption rate of the PEMFC; and $S_{H_2}$ is the stoichiometric ratio of hydrogen supplied.

The power consumption of the auxiliary machine com-

posed of the pump and control system of PEMFC is not negligible. The power consumption of the auxiliary machine can be fitted according to the experimental data as follows:

$$P_{\text{aux}}^{\text{fc}} = k_5 P_{\text{fc}}^5 + k_4 P_{\text{fc}}^4 + k_3 P_{\text{fc}}^3 + k_2 P_{\text{fc}}^2 + k_1 P_{\text{fc}} + k_0 \tag{19}$$

where $k_0$-$k_5$ are the auxiliary power fitting coefficients of PEMFC.

According to (18) and (19), the net output power of PEMFC can be obtained as:

$$P_{\text{net}}^{\text{fc}} = P_{\text{fc}} - P_{\text{aux}}^{\text{fc}} \tag{20}$$

According to the conservation of mass and energy, the heat generation of the reaction process can be calculated by the difference between the reaction enthalpy of the substance entering and leaving the PEMFC as follows:

$$Q_{\text{fc}} = H_{\text{H}_2}^{\text{anin}} + H_{\text{air}}^{\text{cain}} - H_{\text{H}_2}^{\text{anout}} - H_{\text{air}}^{\text{caout}} - H_{\text{H}_2\text{O}}^{\text{anout}} - H_{\text{H}_2\text{O}}^{\text{caout}} - P_{\text{fc}} \tag{21}$$

where $Q_{\text{fc}}$ is the heat generation power of PEMFC; $H_{\text{H}_2}^{\text{anin}}$ and $H_{\text{H}_2}^{\text{anout}}$ are the reaction enthalpies of hydrogen entering and leaving the anode, respectively; $H_{\text{air}}^{\text{cain}}$ and $H_{\text{air}}^{\text{caout}}$ are the reaction enthalpies of air entering and leaving the cathode, respectively; and $H_{\text{H}_2\text{O}}^{\text{anout}}$ and $H_{\text{H}_2\text{O}}^{\text{caout}}$ are the reaction enthalpies of water leaving the anode and the cathode, respectively.

The waste heat recovery power is as follows:

$$Q_{\text{fc}}^{\text{rec}} = \left(Q_{\text{fc}} - Q_{\text{dis}}^{\text{fc}}\right)\eta_{\text{rec}} \tag{22}$$

where $Q_{\text{dis}}^{\text{fc}}$ is the heat dissipation power of PEMFC to the surrounding environment.

The technical parameters of the G80pro commercial PEMFC, as shown in Table II, are used for the scheduling simulation. The operating characteristics of PEMFC are presented in Fig. 4.

TABLE II
TECHNICAL PARAMETERS OF G80PRO COMMERCIAL PEMFC

| Parameter | Value |
|---|---|
| Rated power | 77 kW |
| Anode pressure | 1.6 bar |
| Cathode pressure | 1.5 bar |
| Inlet temperature | 72 °C |
| Outlet temperature | 74 °C |
| Stoichiometric ratio of hydrogen | 1.1 |
| Stoichiometric ratio of air | 1.8 |
| Membrane area | 330 $\text{cm}^2$ |
| Number of single-cell series | 210 |
| $ASR$ | 0.05 $\Omega\cdot\text{cm}^2$ |
| $f_1$ | –0.9514 |
| $f_2$ | 0.0034 |
| $f_3$ | $6.9\times10^{-5}$ |
| $f_4$ | $-1.18\times10^{-4}$ |
| $m$ | $2.12\times10^{-5}$ |
| $n$ | $6.35\times10^{-3}$ |
| $k_0$ | 0.7548 |
| $k_1$ | 0.1047 |
| $k_2$ | –0.0012 |
| $k_3$ | $2.3190\times10^{-5}$ |
| $k_4$ | $-1.2236\times10^{-8}$ |
| $k_5$ | $-2.9447\times10^{-10}$ |

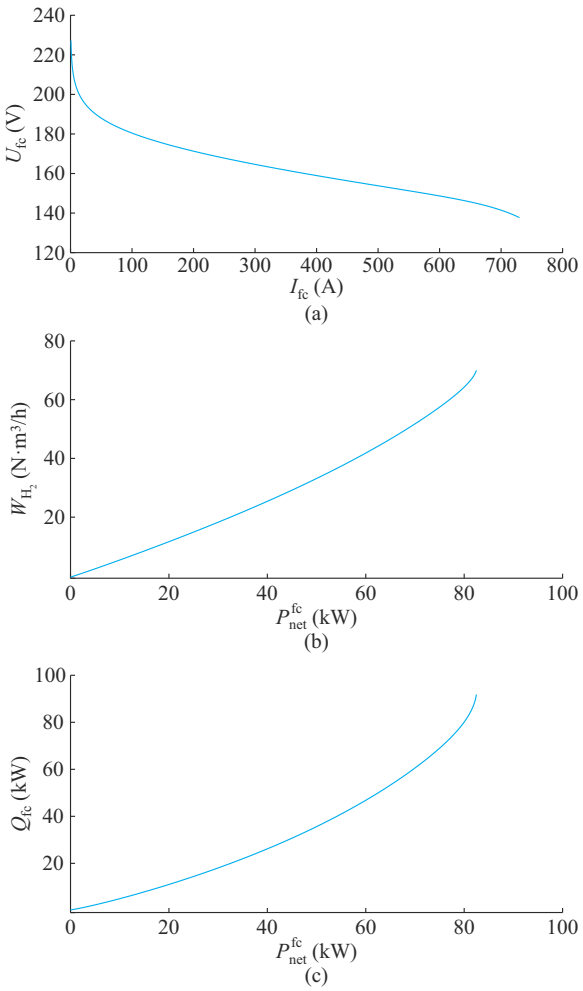


Fig. 4. Operating characteristics of PEMFC. (a) *U-I* characteristic. (b) Hydrogen consumption characteristic. (c) Heat generation characteristic.

PEMFC has a high operating voltage under light load, and long-term operation under light load accelerates the degradation of membrane electrode performance. Furthermore, because of the limitations of heating network conditions, the minimum heat generation power of PEMFC is 40 kW. According to the electrothermal coupling relationship in Fig. 4(c), the actual net output power of PEMFC is limited to the range of 49-67 kW. Within this range, its operating characteristics are close to linear. The linearized hydrogen consumption and heat generation characteristics are expressed as:

$$W_{\text{H}_2} = c_3 P_{\text{net}}^{\text{fc}} + d_3 \tag{23}$$

$$Q_{\text{fc}} = c_4 P_{\text{net}}^{\text{fc}} + d_4 \tag{24}$$

where $c_3$, $c_4$, $d_3$, and $d_4$ are the linear fitting coefficients, which are set as $c_3=0.891$, $d_3=-11.2$, $c_4=1.34$, $d_4=-26$ in this paper. Figure 5 displays a comparison between the linearized and the original model of PEMFC. The maximum error rate of hydrogen consumption is less than 1%, and the maximum error rate of heat generation is less than 1.5%.

### C. Operation Model of Hydrogen Compressor

After passing through the buffer tank and purification device, the hydrogen produced by AEL is pressurized by the

hydrogen compressor and stored in a high-pressure hydrogen storage tank.

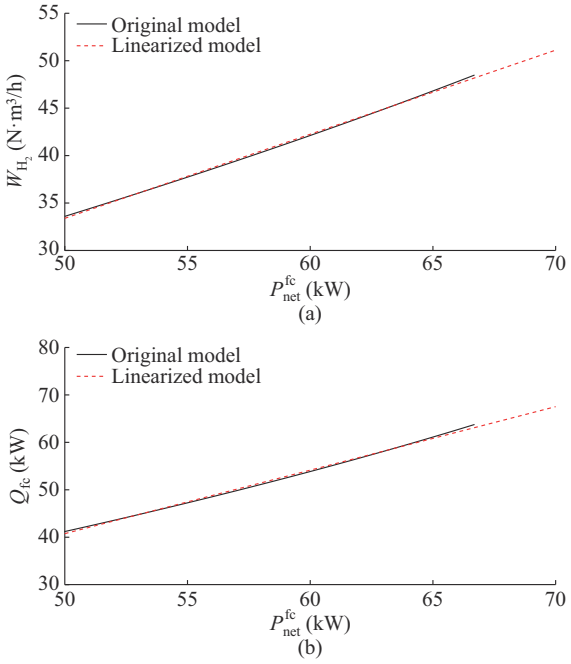


Fig. 5. Comparison of linearized model with original model of PEMFC. (a) Hydrogen consumption characteristic. (b) Heat generation characteristic.

The working pressure of the hydrogen storage tank is 45 MPa, and a 45 MPa two-stage hydrogen compressor is selected for completing the hydrogen pressurization process. Assuming that the compression process of hydrogen is adiabatic compression, the power consumption of the two-stage hydrogen compressor can be expressed as:

$$P_{\text{comp}} = \frac{2N_{\text{H}_2}(1-\gamma)nRT_{\text{in}}}{(n-1)\eta_{\text{comp}}}\left[\left(\frac{P_{\text{out}}}{P_{\text{in}}}\right)^{\frac{n-1}{2n}} - 1\right] \tag{25}$$

where $n$ is the adiabatic exponent of hydrogen compression; $\gamma$ is the loss ratio in the hydrogen purification process; $T_{\text{in}}$ is the temperature of the gas entering the compressor; $P_{\text{in}}$ and $P_{\text{out}}$ are the suction pressure and exhaust pressure of the compressor, respectively; and $\eta_{\text{comp}}$ is the efficiency of the compressor, generally between 0.45 and 0.75 [27].

### D. Operation Model of Hydrogen Storage Tank

The working pressure of the hydrogen storage tank is a state variable. The state of hydrogen-storage (SOH) value of the tank is defined as the ratio of the actual working pressure of the hydrogen storage tank $P_{\text{tank}}$ to the rated pressure $P_{\text{ntank}}$, which is calculated as:

$$SOH = \frac{P_{\text{tank}}}{P_{\text{ntank}}} \tag{26}$$

According to the modified standard gas equation, the operation model of the hydrogen storage tank can be expressed by the change of *SOH* as follows:

$$SOH_{k+1} = SOH_k + z\frac{\left(N_k^{\text{gasin}} - N_k^{\text{gasout}}\right)T_{\text{s}}RT_{\text{tank}}}{V_{\text{tank}}P_{\text{ntank}}} \tag{27}$$

where $SOH_k$ is the SOH value of the $k^{\text{th}}$ time period; $N_k^{\text{gasin}}$ and $N_k^{\text{gasout}}$ are the gas inlet and outlet flow rates of the hydrogen storage tank during the $k^{\text{th}}$ time period, respectively; $z$ is the compression factor of hydrogen; $T_{\text{tank}}$ is the working temperature of the hydrogen storage tank; $V_{\text{tank}}$ is the volume of the hydrogen storage tank; and $T_{\text{s}}$ is the time step of the optimal scheduling.

### E. Operation Model of BESS

For the BESS, the state of charge (SOC) value is typically used to describe its operating state. The operating model of the BESS can be expressed as:

$$SOC_{k+1} = SOC_k + \frac{\eta_{\text{bc}}P_k^{\text{bc}}T_{\text{s}}}{Q_{\text{bat}}} - \frac{P_k^{\text{bd}}T_{\text{s}}}{\eta_{\text{bd}}Q_{\text{bat}}} \tag{28}$$

$$P_k^{\text{bc}}P_k^{\text{bd}} = 0 \tag{29}$$

where $SOC_k$ is the SOC value of the $k^{\text{th}}$ time period; $P_k^{\text{bc}}$ and $P_k^{\text{bd}}$ are the charging power and discharging power during the $k^{\text{th}}$ time period, respectively; $\eta_{\text{bc}}$ and $\eta_{\text{bd}}$ are the charging and discharging efficiencies, respectively; and $Q_{\text{bat}}$ is the capacity of the BESS.

### F. Operation Model of Electric Boiler

The operation model of the electric boiler can be expressed as:

$$Q_{\text{boiler}} = \eta_{\text{boiler}}P_{\text{boiler}} \tag{30}$$

where $Q_{\text{boiler}}$ is the heat generation power of electric boiler; $\eta_{\text{boiler}}$ is the efficiency of the electric boiler; and $P_{\text{boiler}}$ is the rated power of the electric boiler.

## IV. Operation Sequences of HESS

The HESS couples electric energy, heat energy, and hydrogen energy. Therefore, ensuring the safe and reliable operation of HESS is critical. Under the condition of the fluctuating power input of renewable energy, it is difficult to always keep the AEL within the allowable operating load range. When the operating power of the AEL is too low, the lower gas production rate will lead to an increase in the concentration of hydrogen in the oxygen on the anode side. When the concentration of hydrogen in the oxygen on the anode side reaches 2%, the AEL is interlocked and shut down [28], which is not conducive to the continuous operation of AEL. In [29], in the scenario that renewable energy is the primary power supply, the operating states of AEL are categorized into hydrogen production, hot standby, and shutdown states. The cold start of AEL usually takes 1-2 hours [29], which reduces the flexibility of operation. In the hot standby state, AEL can achieve a second-level quick start [30]. The end-user EMS requires that the AEL as a demand response load can significantly change the operating power within 15 min to affect the average energy consumption during this period [31]. Therefore, in order to ensure that AEL can respond quickly to scheduling instructions, AEL should work in hydrogen production or hot standby state, except for maintenance time. When AEL works in hot standby state, its environmental control device needs to consume a certain amount of power to maintain the temperature and pressure balance

of AEL. The power consumed by the environmental control device is related to the ambient temperature. The calculation equation of the heat dissipation power of AEL is given in [32], which is basically negatively correlated with the ambient temperature. According to the parameters of AEL in this paper, the heat dissipation power can be expressed as:

$$Q_{\text{dis}}^{\text{ael}} = \lambda_1 T_{\text{am}} + \lambda_2 \tag{31}$$

where $\lambda_1$ and $\lambda_2$ are the fitting coefficients, and $\lambda_1 = -0.0333$, $\lambda_2 = 3.27$; and $T_{\text{am}}$ is the ambient temperature.

Therefore, the hot standby power of AEL can be expressed as:

$$P_{\text{ael}}^{\text{hotstby}} = \frac{Q_{\text{dis}}^{\text{ael}}}{\eta_{\text{Q}}} + P_{\text{const}}^{\text{stby}} \tag{32}$$

where $P_{\text{const}}^{\text{stby}}$ is the constant standby power of AEL; and $\eta_{\text{Q}}$ is the heating efficiency of the environmental control device.

The high-pressure hydrogen storage tank is a single-port container, which is inflated and deflated by the inlet and outlet valves, respectively, which means that the storage and consumption of hydrogen cannot be carried out at the same time. Besides, multiple conversions between electric and hydrogen energy can reduce the overall energy efficiency and economy of CIES. Therefore, it is necessary to avoid using BESS power generation to produce hydrogen and using PEMFC power generation to charge BESS. From the perspective of the physical constraints of devices, to ensure the flexibility and economy of the system operation, the following operating sequences are formulated for the HESS.

1) Hydrogenation of FCEV and hydrogen production of AEL cannot be performed simultaneously.

2) Power generation of PEMFC and hydrogen production of AEL cannot be performed simultaneously.

3) Power generation of PEMFC and BESS charging cannot be performed simultaneously.

4) BESS discharging and hydrogen production of AEL cannot be performed simultaneously.

Figure 6 displays the operation sequences of HESS, which are the principles that should be followed to ensure the flexibility and economy of CIES.

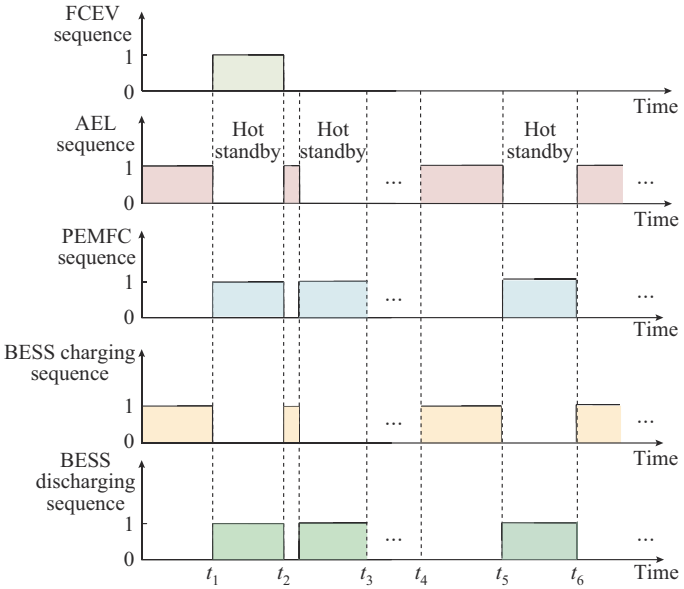


0: Prohibit scheduling or running; 1: Allow scheduling or running

Fig. 6. Operation sequences of HESS.

## V. Model and Constraints of Two-Stage Optimal Scheduling

### A. Optimal Day-ahead Economic Optimization Scheduling Model

#### 1) Objective Function

The optimization objective of CIES connected to the power grid is the transaction cost between the system and the power grid [33], [34]. In this study, in addition to the transaction cost associated with the power grid, the operating cost of the system also considers the cost of using the HESS and BESS, as well as the start-stop cost of HESS to avoid the frequent start-stop of HESS affecting its lifespan. Therefore, the objective function of optimal day-ahead economic optimization scheduling of CIES can be expressed as:

$$\min_{\boldsymbol{X}} \left( C_{\text{grid}} + C_{\text{HESS}} + C_{\text{BESS}} + C_{\text{ael, onoff}} + C_{\text{fc, onoff}} \right) \tag{33}$$

$$C_{\text{grid}} = \sum_{t=1}^{24} C_t^{\text{gridbuy}} P_t^{\text{gridbuy}} T_{\text{s}} - \sum_{t=1}^{24} C_t^{\text{gridsell}} P_t^{\text{gridsell}} T_{\text{s}} \tag{34}$$

$$C_{\text{HESS}} = \sum_{t=1}^{24} \left( \frac{C_{\text{cap}}^{\text{ael}}}{N_{\text{h}}^{\text{ael}}} \delta_t^{\text{ael}} + C_{\text{om}}^{\text{ael}} N_{\text{H}_2,t} \right) T_{\text{s}} + \sum_{t=1}^{24} \frac{C_{\text{cap}}^{\text{fc}}}{N_{\text{h}}^{\text{fc}}} \delta_t^{\text{fc}} T_{\text{s}} \tag{35}$$

$$C_{\text{BESS}} = \sum_{t=1}^{24} \left( \frac{C_{\text{cap}}^{\text{bat}}}{2N_{\text{cycles}}^{\text{bat}}} P_t^{\text{bc}} + \frac{C_{\text{cap}}^{\text{bat}}}{2N_{\text{cycles}}^{\text{bat}}} P_t^{\text{bd}} \right) T_{\text{s}} \tag{36}$$

$$C_{\text{ael, onoff}} = \sum_{t=2}^{24} \frac{\alpha}{2} \left| \delta_t^{\text{ael}} - \delta_{t-1}^{\text{ael}} \right| \tag{37}$$

$$C_{\text{fc, onoff}} = \sum_{t=2}^{24} \frac{\beta}{2} \left| \delta_t^{\text{fc}} - \delta_{t-1}^{\text{fc}} \right| \tag{38}$$

$$\begin{aligned} \boldsymbol{X} = \big[ & P_t^{\text{gridbuy}}, P_t^{\text{gridsell}}, P_t^{\text{bc}}, P_t^{\text{bd}}, P_t^{\text{ael}}, P_t^{\text{fcnet}}, P_t^{\text{boiler}}, P_t^{\text{comp}}, \\ & P_t^{\text{hotstby}}, P_t^{\text{aelaux}}, \delta_t^{\text{bc}}, \delta_t^{\text{bd}}, \delta_t^{\text{ael}}, \delta_t^{\text{fc}}, \delta_t^{\text{fcev}}, \delta_t^{\text{gridbuy}}, \delta_t^{\text{gridsell}} \big] \end{aligned} \tag{39}$$

where $\boldsymbol{X}$ is the decision variable; $C_{\text{grid}}$ is the transaction cost between the CIES and power grid; $C_t^{\text{gridbuy}}$ and $C_t^{\text{gridsell}}$ are the purchase and sale prices of electricity to power grid, respectively; $P_t^{\text{gridbuy}}$ and $P_t^{\text{gridsell}}$ are the power purchased from and sold to the power grid, respectively; $C_{\text{HESS}}$ is the cost of using the HESS; $C_{\text{cap}}^{\text{ael}}$ is the investment cost of AEL; $C_{\text{cap}}^{\text{fc}}$ is the investment cost of PEMFC; $C_{\text{om}}^{\text{ael}}$ is the operating cost of AEL, which is the cost of water consumed; $N_{\text{h}}^{\text{ael}}$ and $N_{\text{h}}^{\text{fc}}$ are the service lifespans of AEL and PEMFC, respectively; $\delta_t^{\text{ael}}$ and $\delta_t^{\text{fc}}$ are the binary flag bits of AEL and PEMFC working status, respectively; $C_{\text{BESS}}$ is the cost of using the BESS; $C_{\text{cap}}^{\text{bat}}$ is the investment cost of BESS; $N_{\text{cycles}}^{\text{bat}}$ is the cycle life of BESS; $P_t^{\text{bc}}$ and $P_t^{\text{bd}}$ are the charging power and discharging power, respectively; $C_{\text{ael,onoff}}$ is the start-stop cost of AEL; $C_{\text{fc,onoff}}$ is the start-stop cost of PEMFC; $P_t^{\text{ael}}$ is the hydrogen production power of AEL; $P_t^{\text{fcnet}}$ is the net output power of PEMFC; $P_t^{\text{boiler}}$ is the power of electric boiler; $P_t^{\text{comp}}$ is the power of the hydrogen compressor; $P_t^{\text{hotstby}}$ is the hot standby power of AEL; $P_t^{\text{aelaux}}$ is the auxiliary power of AEL; $\delta_t^{\text{bc}}$ and

$\delta_t^{\mathrm{bd}}$ are the binary variables for charging and discharging of BESS, respectively; $\delta_t^{\mathrm{fcev}}$ is the binary variable for the hydrogen charging of FCEV; $\delta_t^{\mathrm{gridbuy}}$ and $\delta_t^{\mathrm{gridsell}}$ are the binary variables for purchasing and selling electricity from the power grid, respectively; $\alpha$ is the single start-stop cost of AEL; and $\beta$ is the single start-stop cost of PEMFC.

*2) Constraints*

Formula (40) is the operating load constraint of AEL. Formula (41) is the power consumption of the purification, separation, and auxiliary devices of AEL. Formula (42) is the constraint of waste heat recovery power of AEL. Formulas (43)-(46) are the operational sequence constraints of AEL. Formulas (47) and (48) are the operational load constraint and waste heat recovery power constraint of PEMFC, respectively. Formula (50) is the operational sequence constraint of PEMFC. Formula (51) is the operational constraint of hydrogen compressor. Formula (52) is the operational constraint of hydrogen storage tank. Formulas (53)-(57) are the operational constraints of BESS. Formula (58) is the operational constraint of electric boiler. Formulas (59)-(61) are the operational constraints for the interaction between the CIES and power grid. Formulas (62)-(64) are the balance constraints of electric energy, thermal energy, and hydrogen energy in the system, respectively. Formulas (65) and (66) are the continuity constraints of the day-ahead economic optimization scheduling.

$$\delta_t^{\mathrm{ael}} P_{\min}^{\mathrm{ael}} \le P_t^{\mathrm{ael}} \le \delta_t^{\mathrm{ael}} P_{\max}^{\mathrm{ael}} \tag{40}$$

$$P_t^{\mathrm{aelaux}} = \xi_{\mathrm{aux}} P_t^{\mathrm{ael}} \tag{41}$$

$$Q_{\min}^{\mathrm{rec}} \le Q_{\mathrm{ael}}^{\mathrm{rec}} \le Q_{\max}^{\mathrm{rec}} \tag{42}$$

$$P_t^{\mathrm{hotstby}} = \left(1 - \delta_t^{\mathrm{ael}}\right) P_{\mathrm{ael}}^{\mathrm{hotstby}} \tag{43}$$

$$0 \le \delta_t^{\mathrm{ael}} + \delta_t^{\mathrm{fc}} \le 1 \tag{44}$$

$$0 \le \delta_t^{\mathrm{ael}} + \delta_t^{\mathrm{fcev}} \le 1 \tag{45}$$

$$0 \le \delta_t^{\mathrm{ael}} + \delta_t^{\mathrm{bd}} \le 1 \tag{46}$$

$$\delta_t^{\mathrm{fc}} P_{\min}^{\mathrm{fc}} \le P_t^{\mathrm{fcnet}} \le \delta_t^{\mathrm{fc}} P_{\max}^{\mathrm{fc}} \tag{47}$$

$$Q_{\min}^{\mathrm{rec}} \le Q_{\mathrm{fc}}^{\mathrm{rec}} \le Q_{\max}^{\mathrm{rec}} \tag{48}$$

$$0 \le \delta_t^{\mathrm{fc}} + \delta_t^{\mathrm{gridsell}} \le 1 \tag{49}$$

$$0 \le \delta_t^{\mathrm{fc}} + \delta_t^{\mathrm{bc}} \le 1 \tag{50}$$

$$0 \le P_t^{\mathrm{comp}} \le P_{\max}^{\mathrm{comp}} \tag{51}$$

$$SOH_t^{\min} \le SOH_t \le SOH_t^{\max} \tag{52}$$

$$0 \le P_t^{\mathrm{bc}} \le \delta_t^{\mathrm{bc}} P_{\max}^{\mathrm{bc}} \tag{53}$$

$$0 \le P_t^{\mathrm{bd}} \le \delta_t^{\mathrm{bd}} P_{\max}^{\mathrm{bd}} \tag{54}$$

$$0 \le \delta_t^{\mathrm{bc}} + \delta_t^{\mathrm{bd}} \le 1 \tag{55}$$

$$0 \le \delta_t^{\mathrm{bd}} + \delta_t^{\mathrm{gridsell}} \le 1 \tag{56}$$

$$SOC_t^{\min} \le SOC_t \le SOC_t^{\max} \tag{57}$$

$$0 \le P_t^{\mathrm{boiler}} \le P_{\max}^{\mathrm{boiler}} \tag{58}$$

$$0 \le P_t^{\mathrm{gridbuy}} \le \delta_t^{\mathrm{gridbuy}} P_{\max}^{\mathrm{grid}} \tag{59}$$

$$0 \le P_t^{\mathrm{gridsell}} \le \delta_t^{\mathrm{gridsell}} P_{\max}^{\mathrm{grid}} \tag{60}$$

$$0 \le \delta_t^{\mathrm{gridbuy}} + \delta_t^{\mathrm{gridsell}} \le 1 \tag{61}$$

$$P_t^{\mathrm{PV}} + P_t^{\mathrm{bd}} + P_t^{\mathrm{gridbuy}} + P_t^{\mathrm{fcnet}} = P_t^{\mathrm{bc}} + P_t^{\mathrm{ael}} + P_t^{\mathrm{boiler}} + P_t^{\mathrm{load}} + P_t^{\mathrm{comp}} + P_t^{\mathrm{gridsell}} + P_t^{\mathrm{hotstby}} + P_t^{\mathrm{aelaux}} \tag{62}$$

$$Q_t^{\mathrm{fcrec}} + Q_t^{\mathrm{aelrec}} + Q_t^{\mathrm{boiler}} = Q_t^{\mathrm{load}} \tag{63}$$

$$\Delta N_t^{\mathrm{tank}} = \Delta N_t^{\mathrm{ael}} \left(1 - \gamma\right) \delta_t^{\mathrm{ael}} - \Delta N_t^{\mathrm{fc}} \delta_t^{\mathrm{fc}} - \Delta N_t^{\mathrm{fcev}} \tag{64}$$

$$SOC_0 = SOC_{24} \tag{65}$$

$$SOH_0 = SOH_{24} \tag{66}$$

where $P_{\min}^{\mathrm{ael}}$ and $P_{\max}^{\mathrm{ael}}$ are the minimum and maximum operating power of AEL, respectively; $\xi_{\mathrm{aux}}$ is the ratio of auxiliary power consumption to hydrogen production power consumption; $Q_{\min}^{\mathrm{rec}}$ and $Q_{\max}^{\mathrm{rec}}$ are the minimum and maximum recoverable thermal power determined by the heating network, respectively; $P_{\min}^{\mathrm{fc}}$ and $P_{\max}^{\mathrm{fc}}$ are the minimum and maximum net output power of PEMFC, respectively; $P_{\max}^{\mathrm{comp}}$ is the rated power of hydrogen compressor; $SOH_t^{\min}$ and $SOH_t^{\max}$ are the minimum and maximum SOH values of the hydrogen storage tank, respectively; $P_{\max}^{\mathrm{bc}}$ and $P_{\max}^{\mathrm{bd}}$ are the maximum charging and discharging power of BESS, respectively; $SOC_t^{\min}$ and $SOC_t^{\max}$ are the minimum and maximum SOC values of BESS, respectively; $P_{\max}^{\mathrm{boiler}}$ is the rated power of the electric boiler; $P_{\max}^{\mathrm{grid}}$ is the maximum power of grid interaction; $Q_t^{\mathrm{fcrec}}$ and $Q_t^{\mathrm{aelrec}}$ are the waste heat recovery power of PEMFC and AEL, respectively; $Q_t^{\mathrm{boiler}}$ is the heat generation power of electric boiler; $Q_t^{\mathrm{load}}$ is the power of heat load; $\Delta N_t^{\mathrm{tank}}$ is the hydrogen molar change of hydrogen storage tank during $T_{\mathrm{s}}$; $\Delta N_t^{\mathrm{ael}}$ is the molar amount of hydrogen production during $T_{\mathrm{s}}$; $\Delta N_t^{\mathrm{fc}}$ is the molar amount of hydrogen consumed by PEMFC during $T_{\mathrm{s}}$; $\Delta N_t^{\mathrm{fcev}}$ is the molar amount of hydrogen consumed by FCEV during $T_{\mathrm{s}}$; $SOC_0$ and $SOC_{24}$ are the SOC values of BESS at the beginning and end of the day, respectively; and $SOH_0$ and $SOH_{24}$ are the SOH values of the hydrogen storage tank at the beginning and end of the day, respectively.

Combining (33)-(66), the optimal day-ahead economic optimization scheduling problem of CIES is formulated as a mixed-integer linear programming (MILP) problem.

### *B. Optimal Intra-day Rolling Optimization Scheduling Model*

The optimal day-ahead economic optimization scheduling is based on the predicted PV power and load at the 1-hour time scale, combined with the electricity market price, and provides a economic scheduling plan. However, the day-ahead prediction data exhibit a greater prediction error compared with the intra-day ultra-short time-scale prediction data. Overly extensive scheduling can lead to the poor reliability of load power supply. To reduce the uncertainty of the actual operation of the system caused by the source-load prediction error and achieve accurate scheduling, based on the intra-day ultra-short time-scale PV power and load prediction data, the HESS, BESS, and electric boiler are considered to balance power fluctuation in the intra-day ultra-short time scale through rolling optimization to realize the optimal control of system power balance and make load supply more

reliable.

Figure 7 displays the principle of two-stage optimal scheduling.

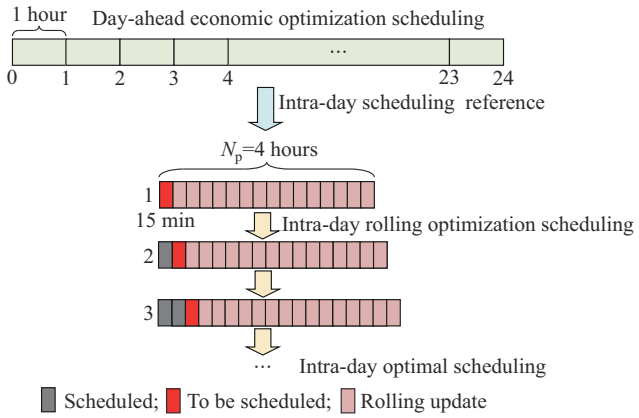


Fig. 7. Principle of two-stage optimal scheduling.

The prediction period of the intra-day rolling optimization scheduling $N_p$ is the ultra-short time-scale prediction period of PV and load, which is 4 hours, and the rolling time step is 15 min. In intra-day rolling optimization scheduling process, the day-ahead economic optimization scheduling instructions are used as the reference. The objective function of the intra-day rolling optimization scheduling is expressed as:

$$\min_{\boldsymbol{X}} \left( C_{\text{Pael}}^{\text{penalty}} + C_{\text{Pfc}}^{\text{penalty}} + C_{\text{Pbat}}^{\text{penalty}} + C_{\text{Pboiler}}^{\text{penalty}} \right) \tag{67}$$

$$C_{\text{Pael}}^{\text{penalty}} = \sum_{k=1}^{N_p} \left( P_k^{\text{ael}} - P_t^{\text{ael}} \right)^2 \tag{68}$$

$$C_{\text{Pfc}}^{\text{penalty}} = \sum_{k=1}^{N_p} \left( P_k^{\text{fcnet}} - P_t^{\text{fcnet}} \right)^2 \tag{69}$$

$$C_{\text{Pbat}}^{\text{penalty}} = \sum_{k=1}^{N_p} \left[ \left( P_k^{\text{bc}} - P_k^{\text{bd}} \right) - \left( P_t^{\text{bc}} - P_t^{\text{bd}} \right) \right]^2 \tag{70}$$

$$C_{\text{Pboiler}}^{\text{penalty}} = \sum_{k=1}^{N_p} \left( P_k^{\text{boiler}} - P_t^{\text{boiler}} \right)^2 \tag{71}$$

$$\begin{aligned} \boldsymbol{X} = \big[ & P_k^{\text{gridbuy}}, P_k^{\text{gridsell}}, P_k^{\text{bc}}, P_k^{\text{bd}}, P_k^{\text{ael}}, P_k^{\text{fcnet}}, P_k^{\text{boiler}}, P_k^{\text{comp}}, \\ & P_k^{\text{hotstby}}, P_k^{\text{aelaux}}, \delta_k^{\text{bc}}, \delta_k^{\text{bd}}, \delta_k^{\text{ael}}, \delta_k^{\text{fc}}, \delta_k^{\text{fcev}}, \delta_k^{\text{gridbuy}}, \delta_k^{\text{gridsell}} \big] \end{aligned} \tag{72}$$

where $C_{\text{Pael}}^{\text{penalty}}$, $C_{\text{Pfc}}^{\text{penalty}}$, $C_{\text{Pbat}}^{\text{penalty}}$, and $C_{\text{Pboiler}}^{\text{penalty}}$ are the power adjustment penalties of AEL, PEMFC, BESS, and electric boilers, respectively; and $k$ denotes the $k^{\text{th}}$ time period. The variables with subscript $k$ and the corresponding variables with subscript $t$ are defined in a similar manner and thus not explained further here.

The constraints of intra-day rolling optimization scheduling are the same as those of the day-ahead stage, as shown in (40)-(64). Due to the rapid power ramp rates of AEL and PEMFC, a steady state of power can be achieved within the intra-day rolling optimization scheduling time step. Therefore, their power ramping constraints are not considered in the two-stage optimal scheduling. Combining (67)-(72), the optimal intra-day rolling optimization scheduling problem can be simplified to a mixed-integer quadratic programming (MIQP) problem.

## VI. Simulation Result

The two-stage optimal scheduling model of CIES is simulated and validated using the Cplex commercial solver based on the MATLAB platform. Table III presents the simulation parameters of the system.

TABLE III
Simulation Parameters of System

| Parameter | Value | Parameter | Value |
|---|---|---|---|
| $P_{\max}^{\text{PV}}$ | 700 kWp | $\eta_{\text{boiler}}$ | 0.9 |
| $P_{\max}^{\text{ael}}$ | 190 kW | $\eta_{\text{bc}}$ | 0.95 |
| $P_{\min}^{\text{ael}}$ | 84 kW | $\eta_{\text{bd}}$ | 0.97 |
| $P_{\max}^{\text{fc}}$ | 67 kW | $\eta_{\text{rec}}$ | 0.86 |
| $P_{\min}^{\text{fc}}$ | 49 kW | $P_{\max}^{\text{grid}}$ | 1.5 MW |
| $P_{\max}^{\text{boiler}}$ | 200 kW | $N_{\text{cycles}}^{\text{bat}}$ | 3000 |
| $P_{\max}^{\text{bc}}$ | 1 MW | $C_{\text{cap}}^{\text{fc}}$ | 385000 CNY |
| $P_{\max}^{\text{bd}}$ | 1 MW | $N_{\text{h}}^{\text{fc}}$ | 30000 hours |
| $P_{\max}^{\text{comp}}$ | 10 kW | $C_{\text{cap}}^{\text{ael}}$ | 280000 CNY |
| $V_{\text{tank}}$ | 5 m$^3$ | $N_{\text{h}}^{\text{ael}}$ | 200000 hours |
| $SOH_{\min}$ | 0.05 | $z$ | 1.1 |
| $SOH_{\max}$ | 1 | $C_{\text{om}}^{\text{ael}}$ | 0.01 CNY/(N·m$^3$) |
| $SOC_{\min}$ | 0.2 | $C_{\text{cap}}^{\text{bat}}$ | 1500 CNY/kWh |
| $SOC_{\max}$ | 0.85 | $\xi_{\text{aux}}$ | 0.09 |
| $Q_{\text{bat}}$ | 2 MWh | $\alpha$ | 25 CNY |
| $P_{\text{ntank}}$ | 45 MPa | $\beta$ | 10 CNY |
| $P_{\text{const}}^{\text{stby}}$ | 12 kW | $\gamma$ | 0.08 |

The distributed PV power generation in the CIES preferentially satisfies the local load, and the excess power is absorbed by the power grid. The power purchase price of the power grid follows the time-of-use price issued locally. The subsidy for integrating excess distributed PV power generation into the power grid is 0.1 CNY/kWh. This study conducts the simulation analysis based on PV power generation, load, and time-of-use electricity price data from four typical days in four seasons. Figure 8 shows the simulation data of a typical summer day, where the time step of the sampling point is 15 min.

### A. Optimal Day-ahead Economic Optimization Scheduling Simulation

The optimal day-ahead economic optimization scheduling simulation is performed according to the day-ahead source-load prediction data.

Considering a typical summer day as an example, Fig. 9 displays the optimal day-ahead economic optimization scheduling results. Figure 9(a) shows that because the FCEV needs to supplement hydrogen during the morning period, and considering the incentive of the time-of-use electricity price, the system employs surplus PV power in the afternoon and valley-price electricity from the power grid at night for the production of hydrogen, which is utilized for the hydrogen load.

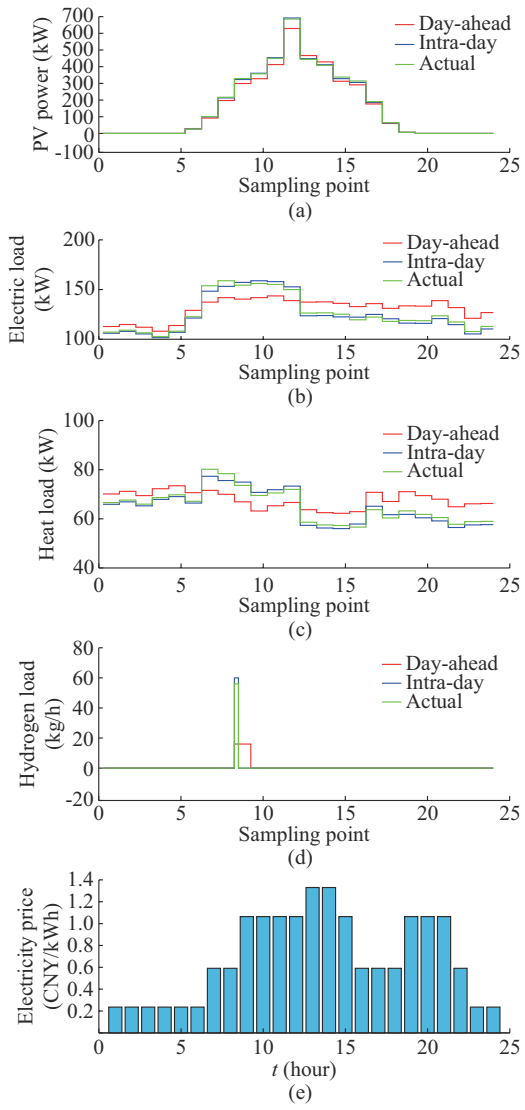


Fig. 8. Simulation data. (a) PV power generation. (b) Electric load. (c) Heat load. (d) Hydrogen load. (e) Time-of-use electricity price.

At night, PV power generation stops, and the BESS and PEMFC use excess electric and hydrogen energy to provide energy to the system during the peak electricity price period to reduce the energy cost of the system. Figure 9(c) shows the changes in the *SOC* of BESS and the *SOH* of hydrogen storage tank in the optimal day-ahead economic optimization scheduling stage. The initial and final values of the *SOC* and *SOH* are equal, which satisfies the continuity requirements of day-ahead economic optimization scheduling. Figure 9(d) reveals that the waste heat recovery of AEL and PEMFC can provide heat energy supplement for the system during most periods of the day and improve the energy utilization rate of the system.

Figure 10 shows the optimal day-ahead economic optimization scheduling results without considering the start-stop costs of HESS in the objective function. It can be observed that the start-stop times and operation time of PEMFC and AEL increase, and the system operating cost also increases from 1052.2 CNY to 1068.1 CNY, which is not conducive to the economic operation of the system.

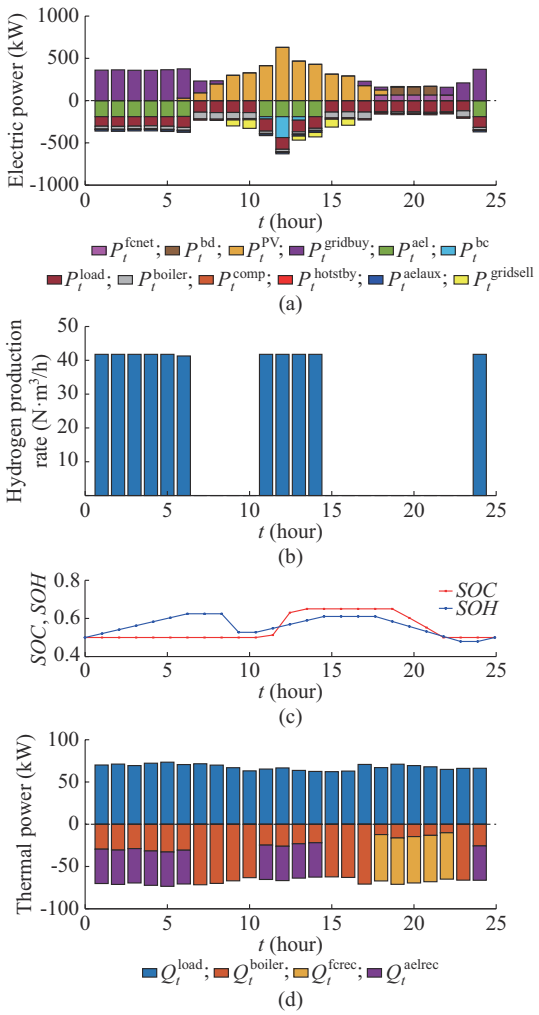


Fig. 9. Optimal day-ahead economic optimization scheduling results. (a) Electric power balance. (b) Hydrogen production rate. (c) *SOC* and *SOH*. (d) Thermal power balance.

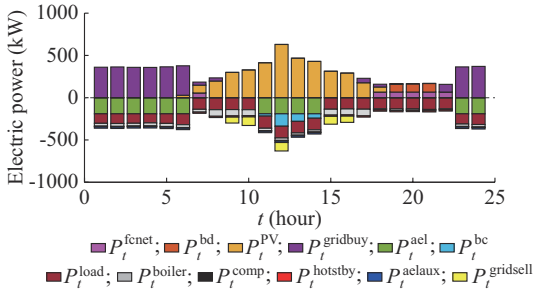


Fig. 10. Optimal day-ahead economic optimization scheduling results without considering start-stop costs of HESS in objective function.

### *B. Optimal Intra-day Rolling Optimization Scheduling Simulation*

The intra-day rolling optimization scheduling is used to achieve accurate scheduling and reduce the effect of uncertainty caused by the source-load prediction error. Figure 11 displays the results of optimal intra-day rolling optimization scheduling, where the time step of the sampling point is 15 min. Compared with the optimal day-ahead economic optimization scheduling in Fig. 9, the optimal intra-day rolling opti-

mization scheduling can respond to load changes in a shorter time scale, maintain the balance of various energy flows in the system, and ensure the accuracy and reliability of the system scheduling.

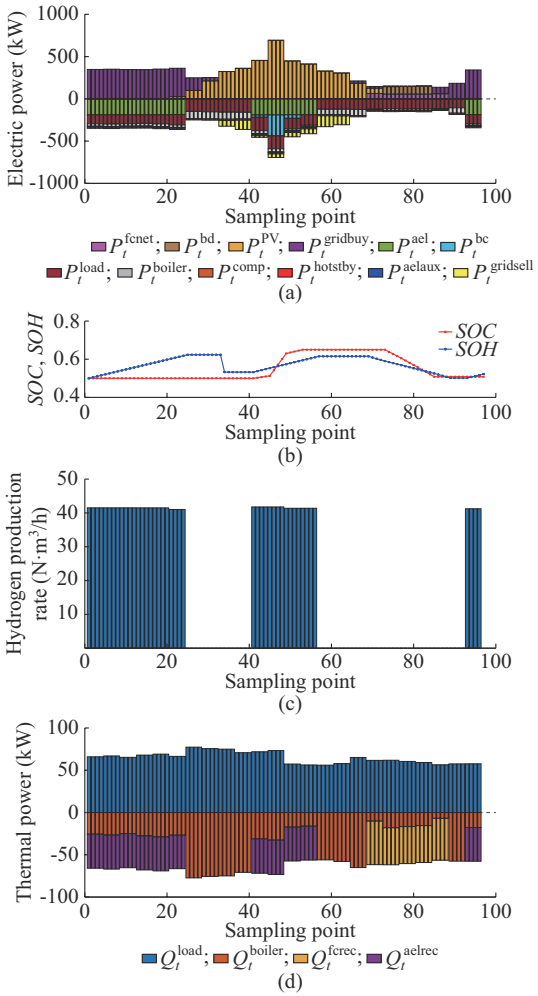


Fig. 11. Optimal intra-day rolling optimization scheduling results. (a) Electric power balance. (b) *SOC* and *SOH*. (c) Hydrogen production rate. (d) Thermal power balance.

In intra-day rolling optimization scheduling, the power fluctuation caused by the day-ahead source-load prediction error is distributed through the real-time power adjustment of the AEL, PEMFC, BESS, electric boiler, and power grid. Figure 12 presents a comparison between the intra-day rolling optimization scheduling power and the day-ahead economic optimization scheduling power of each unit, where the time step of sampling point is 15 min. The source-load prediction data and time-of-use electricity price data of typical days in four seasons were selected to compare the operating costs and load offsets of day-ahead economic optimization scheduling and two-stage optimal scheduling. The load offset is used to measure the reliability of load energy supply, which is defined as:

$$R_{\text{offset}} = \frac{\sum_{i=1}^{96} \left| E_{\text{load},i} - E_{\text{load},i,\text{re}} \right|}{\sum_{i=1}^{96} E_{\text{load},i,\text{re}}} \times 100\% \tag{73}$$

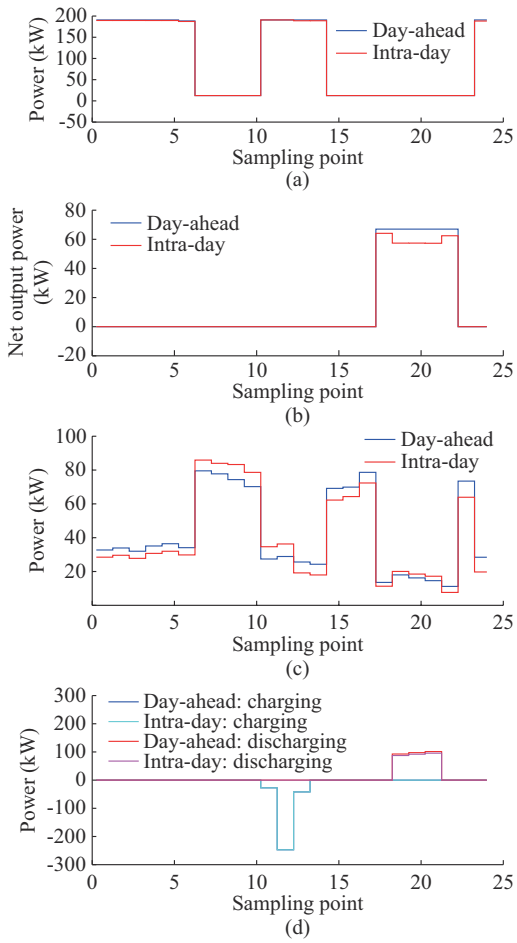


Fig. 12. Comparison of day-ahead economic optimization and intra-day rolling optimization scheduling power. (a) Power of AEL. (b) Net output power of PEMFC. (c) Power of electric boiler. (d) Power of BESS.

where $E_{\text{load},i}$ and $E_{\text{load},i,\text{re}}$ are the actual supply energy and load demand energy within the $i^{\text{th}}$ time step, respectively, and the time step is 15 min.

The optimal day-ahead economic optimization scheduling has an economic significance, but its disadvantage is that the scheduling errors are relatively large. It is difficult to maintain the balance of multiple energy flows in a short time scale. The purpose of the two-stage optimal scheduling with intra-day rolling optimization is to correct the error of day-ahead economic optimization scheduling in real time and improve the reliability of load energy supply. As shown in Table IV, the actual operating costs and load offsets of the two scheduling models are compared. The simulation results show that the two-stage optimal scheduling reduces the total load offset by about 14% while maintaining similar operating cost to the optimal day-ahead economic optimization scheduling, which improves the reliability of the system energy supply.

Finally, this paper analyzes the impact of operation sequences on the economy. In the operation sequences shown in Fig. 6, in addition to the operation sequences determined by the physical characteristics of the devices, the sequences between HESS and BESS can be set flexibly. Table V shows the daily operating costs and load offsets of four typical

days. There are no operation sequence constraints between the HESS and BESS in case 1, and these constraints are set in case 2. Compared with case 1, case 2 reduces the actual operating cost of the system by up to 4.4% while keeping the load offset unchanged. Therefore, considering the operation sequences between the BESS and HESS can reduce the economic loss caused by multiple conversions of electric and hydrogen energy, which is conducive to the economic operation of the system.

TABLE IV
ACTUAL OPERATING COST AND LOAD OFFSETS OF TWO-STAGE OPTIMAL SCHEDULING MODELS

| Season | Model | Operating cost (CNY) | Load offset (%) |
|---|---|---|---|
| Spring | Day-ahead | 1909.3 | 18.18 |
| | Two-stage | 1905.2 | 4.01 |
| Summer | Day-ahead | 1052.2 | 18.26 |
| | Two-stage | 1047.1 | 4.02 |
| Autumn | Day-ahead | 1805.5 | 18.30 |
| | Two-stage | 1804.2 | 4.05 |
| Winter | Day-ahead | 3172.0 | 18.15 |
| | Two-stage | 3166.5 | 4.00 |

TABLE V
OPERATING COST AND LOAD OFFSETS IN FOUR TYPICAL DAYS

| Season | Case | Operating cost (CNY) | Load offset (%) |
|---|---|---|---|
| Spring | 1 | 1988.0 | 4.01 |
| | 2 | 1905.2 | 4.01 |
| Summer | 1 | 1085.4 | 4.02 |
| | 2 | 1047.1 | 4.02 |
| Autumn | 1 | 1884.3 | 4.05 |
| | 2 | 1804.2 | 4.05 |
| Winter | 1 | 3247.1 | 4.00 |
| | 2 | 3166.5 | 4.00 |

## VII. CONCLUSION

Based on the purpose of improving the reliability and economy of CIES with P2HH, a two-stage optimal scheduling model considering HESS operation sequences is proposed in this paper. The conclusions of this study are as follows:

1) According to the actual parameters of HESS, a refined model of HESS is established, which can effectively reflect the electricity-hydrogen-thermal coupling relationships. Based on the operation domain of HESS, the HESS model is linearized. The maximum approximate error of hydrogen production of AEL is less than 2%, and the error of heat production is less than 5%. The error of hydrogen consumption of PEMFC is less than 1%, and the error of heat production is less than 1.5%.

2) In the day-ahead economic optimization scheduling model, the start-stop cost of HESS is considered. On the premise of ensuring the supply of hydrogen load, the number of start-stop times of HESS can be effectively reduced and the scheduling cost can be saved.

3) By formulating the operation sequences of HESS, the scheduling model is more closely aligned with the actual system operation conditions, the flow path of electric energy and hydrogen energy in the system is optimized, and the economic loss caused by multiple energy conversion of electric energy and hydrogen energy is reduced. The operating cost of the system is reduced by up to about 4.4%, which improves the operating economy of CIES.

4) Based on the source-load data and time-of-use electricity price data of typical days in four seasons, the daily operating costs and load offsets of two-stage optimal scheduling and optimal day-ahead economic optimization scheduling are compared. The results show that the two-stage optimal scheduling reduces the load offset by about 14% and improves the reliability of the system energy supply while the actual operating cost is basically the same.

## REFERENCES

[1] X. Kong, R. Wang, Y. Li *et al*., "Optimal operation of a micro-combined cooling, heating and power system driven by a gas engine," *Energy Conversion and Management*, vol. 50, no. 3, pp. 530-538, Mar. 2009.

[2] L. Guo, W. Liu, J. Cai *et al*., "A two-stage optimal planning and design method for combined cooling, heat and power microgrid system," *Energy Conversion and Management*, vol. 74, pp. 433-445, Oct. 2013.

[3] J. Li, G. Li, S. Ma *et al*., "Modeling and simulation of hydrogen energy storage system for power-to-gas and gas-to-power systems," *Journal of Modern Power Systems and Clean Energy*, vol. 11, no. 3, pp. 885-895, May 2023.

[4] L. Kong, J. Yu, and G. Cai, "Modeling, control and simulation of a photovoltaic/hydrogen/supercapacitor hybrid power generation system for grid-connected applications," *International Journal of Hydrogen Energy*, vol. 44, no. 46, pp. 25129-25144, Sept. 2019.

[5] P. García, J. P. Torreglosa, L. M. Fernández *et al*., "Optimal energy management system for stand-alone wind turbine/photovoltaic/hydrogen/battery hybrid system with supervisory control based on fuzzy logic," *International Journal of Hydrogen Energy*, vol. 38, no. 33, pp. 14146-14158, Nov. 2013.

[6] P. Garcia, C. A. Garcia, L. M. Fernandez *et al*., "ANFIS-based control of a grid-connected hybrid system integrating renewable energies, hydrogen and batteries," *IEEE Transactions on Industrial Informatics*, vol. 10, no. 2, pp. 1107-1117, May 2014.

[7] L. Kong, J. Yu, G. Cai *et al*., "Power regulation of off-grid electro-hydrogen coupled system based on model predictive control," *Proceedings of the CSEE*, vol. 41, no. 9, pp. 3139-3149, May 2021.

[8] A. M. Abomazid, N. A. El-Taweel, and H. E. Z. Farag, "Optimal energy management of hydrogen energy facility using integrated battery energy storage and solar photovoltaic systems," *IEEE Transactions on Sustainable Energy*, vol. 13, no. 3, pp. 1457-1468, Jul. 2022.

[9] J. Li, J. Lin, Y. Song *et al*., "Operation optimization of power to hydrogen and heat (P2HH) in ADN coordinated with the district heating network," *IEEE Transactions on Sustainable Energy*, vol. 10, no. 4, pp. 1672-1683, Oct. 2019.

[10] N. Endo, E. Shimoda, K. Goshome *et al*., "Simulation of design and operation of hydrogen energy utilization system for a zero emission building," *International Journal of Hydrogen Energy*, vol. 44, no. 14, pp. 7118-7124, Mar. 2019.

[11] W. Huang, B. Zhang, L. Ge *et al*., "Day-ahead optimal scheduling strategy for electrolytic water to hydrogen production in zero-carbon parks type microgrid for optimal utilization of electrolyzer," *Journal of Energy Storage*, vol. 68, p. 107653, Sept. 2023.

[12] Y. Zheng, S. You, H. W. Bindner *et al*., "Optimal day-ahead dispatch of an alkaline electrolyser system concerning thermal-electric properties and state-transitional dynamics," *Applied Energy*, vol. 307, p. 118091, Feb. 2022.

[13] C. Gao, J. Lin, J. Zeng *et al*., "Wind-photovoltaic co-generation prediction and energy scheduling of low-carbon complex regional integrated energy system with hydrogen industry chain based on copula-MILP," *Applied Energy*, vol. 328, p. 120205, Dec. 2022.

[14] T. Niknam, A. Kavousi-Fard, and A. Ostadi, "Impact of hydrogen production and thermal energy recovery of PEMFCPPs on optimal management of renewable microgrids," *IEEE Transactions on Industrial*

*Informatics*, vol. 11, no. 5, pp. 1190-1197, Oct. 2015.
[15] L. Yao and J. C. Teo, "Optimization of power dispatch with load scheduling for domestic fuel cell-based combined heat and power system," *IEEE Access*, vol. 10, pp. 5968-5979, Jan. 2022.
[16] M. Chen, Z. Shen, L. Wang *et al*., "Intelligent energy scheduling in renewable integrated microgrid with bidirectional electricity-to-hydrogen conversion," *IEEE Transactions on Network Science and Engineering*, vol. 9, no. 4, pp. 2212-2223, Jul. 2022.
[17] W. Xu, Y. Guo, T. Meng *et al*., "Coordinated dispatch based on distributed robust optimization for interconnected urban integrated energy and transmission systems," *Journal of Modern Power Systems and Clean Energy*, vol. 12, no. 3, pp. 840-851, May 2024.
[18] Z. Ma, Y. Zhou, Y. Zheng *et al*., "Distributed robust optimal dispatch of regional integrated energy systems based on ADMM algorithm with adaptive step size," *Journal of Modern Power Systems and Clean Energy*, vol. 12, no. 3, pp. 852-862, May 2024.
[19] H. Chen, L. Gao, Y. Zhang *et al*., "Optimal scheduling strategy of a regional integrated energy system considering renewable energy uncertainty and heat network transmission characteristics," *Energy Reports*, vol. 8, pp. 7691-7703, Nov. 2022.
[20] P. Li, Z. Wang, J. Wang *et al*., "Two-stage optimal operation of integrated energy system considering multiple uncertainties and integrated demand response," *Energy*, vol. 225, p. 120256, Jun. 2021.
[21] Ø. Ulleberg, "Modeling of advanced alkaline electrolyzers: a system simulation approach," *International Journal of Hydrogen Energy*, vol. 28, no. 1, pp. 21-33, Jan. 2003.
[22] F. Garcia-Torres and C. Bordons, "Optimal economical schedule of hydrogen-based microgrids with hybrid storage using model predictive control," *IEEE Transactions on Industrial Electronics*, vol. 62, no. 8, pp. 5195-5207, Aug. 2015.
[23] J. Brauns and T. Turek, "Alkaline water electrolysis powered by renewable energy: a review," *Processes*, vol. 8, no. 2, p. 248, Feb. 2020.
[24] T. Adibi, A. Sojoudi, and S. C. Saha, "Modeling of thermal performance of a commercial alkaline electrolyzer supplied with various electrical currents," *International Journal of Thermofluids*, vol. 13, p. 100126, Feb. 2022.
[25] Z. Sun, N. Wang, Y. Bi *et al*., "Parameter identification of PEMFC model based on hybrid adaptive differential evolution algorithm," *Energy*, vol. 90, pp. 1334-1341, Oct. 2015.
[26] S. Ge and B. Yi, "A mathematical model for PEMFC in different flow modes," *Journal of Power Sources*, vol. 124, no. 1, pp. 1-11, Oct. 2003.
[27] C. Li, X. Zhu, G. Cao *et al*., "Dynamic modeling and sizing optimization of stand-alone photovoltaic power systems using hybrid energy storage technology," *Renewable Energy*, vol. 34, no. 3, pp. 815-826, Mar. 2009.
[28] C. Zhang, J. Wang, Z. Ren *et al*., "Wind-powered 250 kW electrolyzer for dynamic hydrogen production: a pilot study," *International Journal of Hydrogen Energy*, vol. 46, no. 70, pp. 34550-34564, Oct. 2021.
[29] C. Varela, M. Mostafa, and E. Zondervan, "Modeling alkaline water electrolysis for power-to-x applications: a scheduling approach," *International Journal of Hydrogen Energy*, vol. 46, no. 14, pp. 9303-9313, Feb. 2021.
[30] M. Kiaee, A. Cruden, D. Infield *et al*., "Utilisation of alkaline electrolysers to improve power system frequency stability with a high penetration of wind power," *IET Renewable Power Generation*, vol. 8, no. 5, pp. 529-536, Jul. 2014.
[31] J. Eichmann, K. Harrison, and M. Peters, "Novel electrolyzer applications: providing more than just hydrogen," National Renewable Energy Lab. (NREL), Golden, USA, Rep. NREL/TP-5400-61758, Nov. 2014.
[32] R. Qi, J. Li, J. Lin *et al*., "Thermal modeling and controller design of an alkaline electrolysis system under dynamic operating conditions," *Applied Energy*, vol. 332, p. 120551, Feb. 2023.
[33] J. Sun, C. Hu, L. Liu *et al*., "Two-stage correction strategy-based real-time dispatch for economic operation of microgrids," *Chinese Journal of Electrical Engineering*, vol. 8, no. 2, pp. 42-51, Jun. 2022.
[34] W. Hu, Y. Dong, L. Zhang *et al*., "Research on complementarity of multi-energy power systems: a review," *iEnergy*, vol. 2, no. 4, pp. 275-283, Dec. 2023.

**Wei Kong** received the master degree from Shanghai University of Electric Power, Shanghai, China, in 2019, and he is currently working toward the Ph.D degree at the Naval University of Engineering, Wuhan, China. His research interests include hydrogen energy storage system operation control and microgrid stability.

**Kai Sun** received the Ph.D. degree in Department of Electrical Engineering, Tsinghua University, Beijing, China, in 2006. He currently works as an Associate Professor at Tsinghua University. His research interests include new energy generation systems, multi-energy microgrid, and power electronics technology in Energy Internet.

**Jinghong Zhao** received the Ph.D. degree in electrical engineering from the Naval University of Engineering, Wuhan, China, in 2009. He is currently a Professor with the Naval University of Engineering. His research interests include power electronics, and design and control of linear motors.